ANNALS OF GEOPHYSICS, 68, 3, NS335, 2025; doi:10.4401/ag-9235
OPEN ACCESS

Long-term analysis of ERT monitoring data measured on a critical slope above a high-speed railway gallery

Azadeh Hojat[*,1,2], Greta Tresoldi[3], Regina Bianchi[1], Federica Brambilla[1], Luigi Zanzi[1]

(1) Politecnico di Milano, Dipartimento di Ingegneria Civile e Ambientale, Milan, Italy
(2) Shahid Bahonar University of Kerman, Department of Mining Engineering, Kerman, Iran
(3) LSI LASTEM, Settala (MI), Italy

Article history: received December 26, 2024; accepted May, 5, 2025

Abstract

A customized electrical resistivity tomography (ERT) monitoring system was installed on a critical slope above a high-speed railway gallery in March 2022 to monitor the stability condition of the slope. We discuss the results of long-term analysis of the data measured by the system from 24 March 2022 until 21 September 2023. Initial data quality checks were performed to control the quality of the data measured during day and night. We then discuss the optimization of the time-lapse inversion algorithm to generate artifact-free ERT images that can reflect the real distribution of the water content. Using meteorological data, the site-specific model for seasonal variations of the soil temperature at different depths was calibrated and the corresponding resistivity corrections were applied to suppress the effects induced by temperature variations that showed to be important only down to 6 m. Five piezometers were installed along the ERT profile to monitor the water table fluctuations and to correlate the inverted resistivities with piezometric measurements. The complex geology of the site and the complex response of the piezometers to rainfalls suggested focusing the analysis on two target zones identified on ERT images rather than analyzing the average behavior of the resistivity versus the average behavior of the piezometers. A scatterplot for one of these zones, apparently the most sensitive zone to rainfalls and water saturation, was obtained from long-term analysis of the ERT data integrated with the piezometric levels and we could establish a preliminary threshold for addressing excessive water content in this area.

Keywords: ERT monitoring; Hydrogeological risk mitigation; Piezometric level; Slope stability; Time-lapse inversion

1. Introduction

In recent years, geophysical monitoring systems have increasingly helped in near-real-time monitoring of unstable slopes to minimize the negative impacts of hazardous events (e.g., Dahlin et al., 2005; Piegari et al., 2009; Chambers et al., 2009, 2022; Amitrano et al., 2010; Supper et al., 2013; Hojat et al., 2021; Tresoldi et al., 2020;

Whiteley et al., 2021; Zhang et al., 2020, 2021; Watlet et al., 2023). Rainfalls are considered as the main reason for slope instability and thus, landslides to happen. Therefore, there is an increasing demand to develop methods capable of monitoring the hydrogeological conditions of the potentially unstable slopes. Among different geophysical techniques, electrical resistivity tomography (ERT) method is the most efficient technology to be integrated with hydrogeological risk mitigation strategies where water content plays the main role on slope instability. ERT images present the subsurface distribution of electrical resistivity which depends on the characteristics of the subsurface material. The main parameters affecting the resistivity of a material are the porosity, the lithological structure, the salinity of the pore water, and, most importantly, the degree of water saturation (Loke et al., 2013; Moradipour et al., 2016). The relationship between electrical resistivity and water content has made ERT monitoring a viable solution to be used by the authorities responsible in managing critical slopes (Tresoldi et al., 2018, 2019).

In this paper, we address the various challenges encountered in applying the ERT monitoring method on a geologically complex environment representing a critical slope above a high-speed railway gallery. In recent years, several customized ERT monitoring systems have arrived at the technological level of readiness to be installed on critical natural and artificial slopes in order to monitor the hydrogeological risks (e.g., Chambers et al., 2009; Kuras et al., 2015; Tresoldi et al., 2018, 2020; Wilkinson et al., 2022, 2023; Hojat, 2024). Compared to commercial multi-purpose resistivity meters, the customized ERT monitoring systems are constructed according to the specific needs of each site for the number of electrodes, the distance between the electrodes and the maximum injection current required to explore the deepest demanded layers. Optimizing these parameters can considerably reduce the costs of the system. Another important aspect is that the general-purpose commercial resistivimeters are portable and are not adapted for permanent installations while the ERT monitoring systems are thought for long-term operations. Therefore, a customized resistivimeter was installed in March 2022 on a critical slope over an important high-speed railway gallery. The system is still in operation and measures at least two datasets every day. The main objective is to assess changes in resistivity over time to monitor the water circulation in the study site and to understand the response of the site to rainfalls with the perspective of defining the conditions for activating early warning notifications. The specifications of the study site, including its complex geology, pose important challenges in data processing and interpretation of the results. In this study, we present the results of long-term analysis of the data acquired by the ERT monitoring system during March 2022-September 2023.

2. The study site

The study site is located in central Italy where the authorities need to monitor the stability of a slope over a gallery of the high-speed railway (Fig. 1a). This location was selected in order to study the slope stability with particular attention to the variations in water level related to meteorological events. A line of drainage wells parallel to the railway track was installed in the past (June 2004) in the upper part of the slope at about 25 m from the gallery (Fig. 1a) to prevent excessive raise of the water level. The geological region where the site is located has a tectonic origin related to the late phases of the formation of the Apennines. The geomorphology consists mainly of siliciclastic rocks and alluvial deposits from the medium-late Pleistocene and Holocene. There is also a limited presence of volcanic rocks. The study site has never experienced a landslide event, but groundwater fluctuations are observed in the existing drainage wells. Therefore, considering that extreme rainfall events caused by climate changes can cause hydrogeological instabilities, permanent monitoring of the slope over the railway gallery that hosts a train almost every 5 min was considered.

In order to select the position of the permanent ERT monitoring system, several reconnaissance ERT profiles were measured on the slope. Preliminary measurements were carried out using different electrode configurations including the Wenner, the Wenner-Schlumberger and the dipole-dipole arrays. Based on the results of the site reconnaissance and the comments from the authorities, the position to deploy the ERT monitoring profile was selected (Fig. 1a). One main issue considered to locate the ERT profile was an anomalous lower-resistivity zone detected on the preliminary surveys, which was later confirmed by the geological model as a higher permeability zone (Fig. 2). The authorities decided to specifically control the temporal variations of this permeable zone and thus, the midpoint of the ERT monitoring profile was located on this part. The ERT line was then located in the upper part of the slope to prevent as much as possible the electromagnetic interference with the electrical lines of the railway but was kept in between the railway track and the line of the drainage wells. In this way, the monitoring system will also perform a control function on the effectiveness of the drainage system.

The monitoring system supports two 24-electrode multi-cables that are connected to 48 plate electrodes. The current injection circuit allows modulation between 0.001 A and 0.4 A with a resolution of 1 μA on current measurements, while the voltmeter has a resolution of 1 μV with a full scale of +0.47 V and 10 μV with a full scale of +4.7 V. The input impedance of the voltmeter is 1.6×10^{10} Ω, and notch filtering can be applied at the frequency of 50 Hz or 60 Hz. The Wenner electrode configuration with the unit electrode spacing of 3 m was selected for long-term data acquisitions. The anti-rodent cables and the electrodes are placed inside a 0.4 m-deep trench (Fig. 1b) and the raw data are immediately corrected for the effect of the soil covering the electrodes (Hojat et al., 2021). The ERT monitoring system is integrated with a meteorological station (Fig. 1c) including a rain gauge, a temperature sensor to monitor the air temperature, a temperature sensor positioned at 1.5 m depth to monitor the soil temperature, and a temperature sensor inside the box housing the system electronics. All monitoring instrumentations are powered by a 40 Ah battery, recharged by a 60 W solar panel (Fig. 1c). In absence of sun, the energy autonomy of the battery

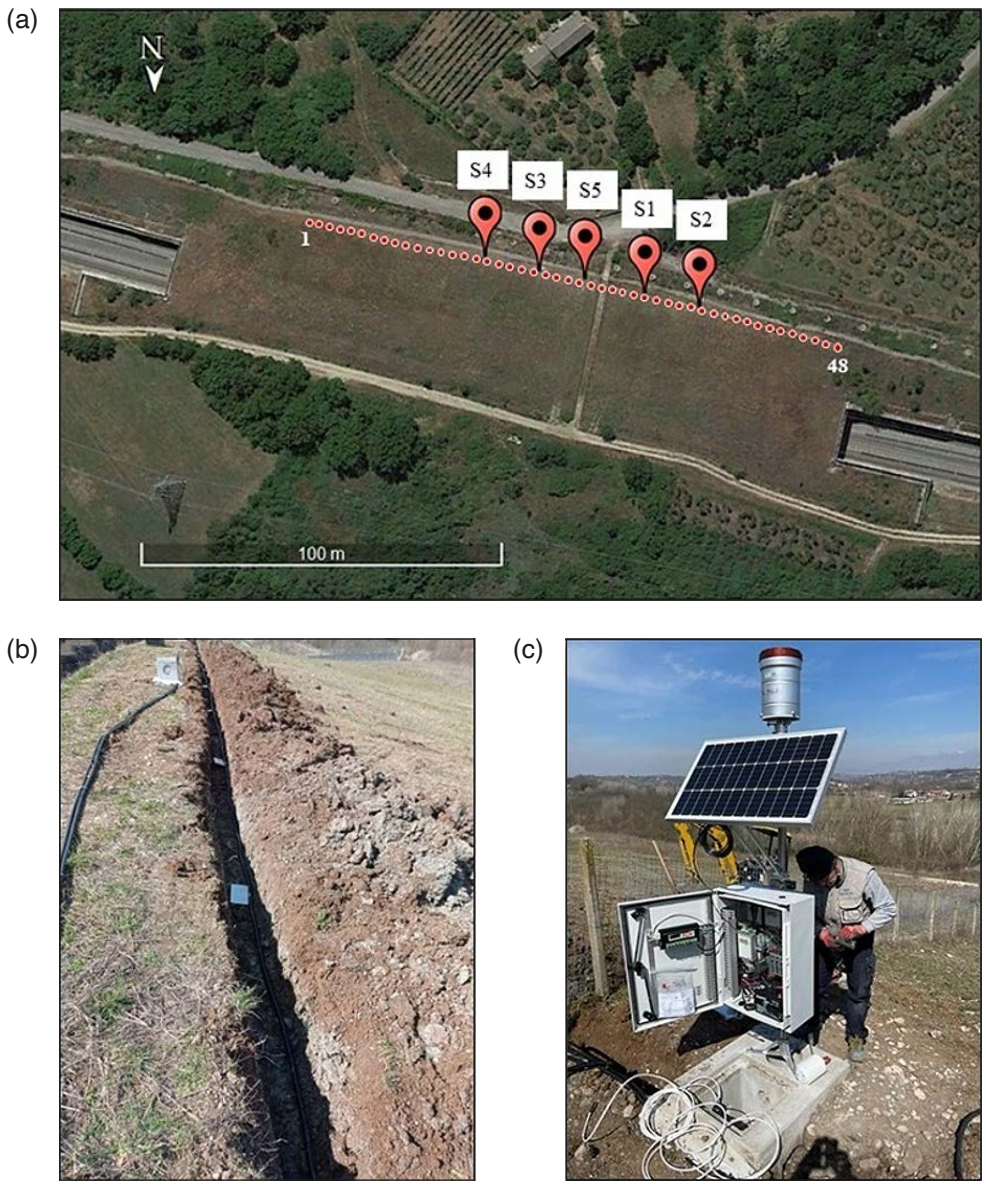

Figure 1. (a) Google view of the study site showing the positions of the electrodes (from 1 to 48) of the ERT monitoring system and the five piezometers S4, S3, S5, S1 and S2 installed along the ERT line. The line of drainage wells pre-existing the installation of the monitoring system is also visible (grey dots aligned along a direction running parallel to the electrode line with a regular spacing of 10 m). (b) Deployment of the cables and electrodes inside a trench. (c) Installing the box housing the electronics of the monitoring system, accompanied by a meteorological station, all powered by a solar panel.

is 10 days. In order to ensure a longer autonomy during prolonged rainy periods, an additional battery pack was installed in March 2023.

In order to obtain detailed geological information, five boreholes were drilled along the ERT line down to a depth of 20 m. Figure 2a illustrates the geological model reconstructed from the analysis of the cores recovered in these boreholes. The boreholes were later used to install five piezometers to monitor the fluctuations of the water table along the ERT line (piezometers S4, S3, S5, S1 and S2 indicated in Fig. 1a). It can be observed in Fig. 2a that the subsurface geology is complex and extremely variable along the ERT profile, particularly for layers deeper than 4 m. The same complexity is also observed in the piezometric levels measured just after the coring operation and during the monitoring period. The geological model of Fig. 2a is superimposed on a typical ERT section on Fig. 2b to demonstrate the variations identified by the resistivity sections. The resistivity values down to about 4 m are smaller than 200 Ωm compatible with the topsoil geological material. The resistivity values of deeper layers increase below the Chaotic Clays. The zone between S1 and S5 is identified by low resistivity values due to a higher piezometric level (about 5 m in S1) observed in the most permeable area. The material surrounding S2 is similar to that hosting S4 apart from the absence of marl blocks and a massive presence of sandy loams.

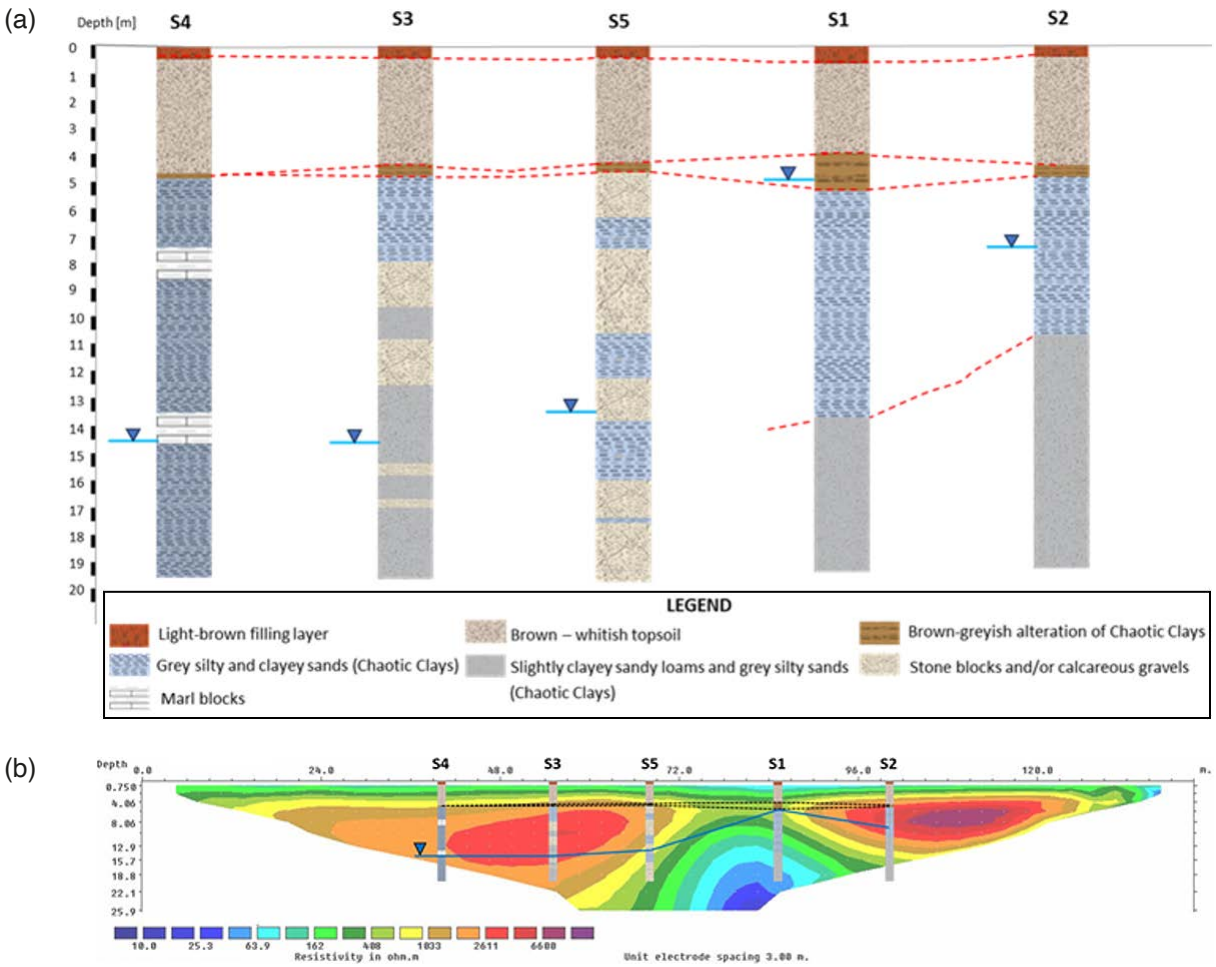

Figure 2. (a) The geological model of the study site defined from coring information sampled along the ERT profile and the piezometric levels in the boreholes after the coring. (b) The geological model superimposed on a typical ERT section.

3. Data processing

The ERT system was installed on 15 March 2022 and we discuss the long-term analysis of the monitoring data for the period 24 March 2022-21 September 2023. In the beginning, we address the complexity of the geological model

that required a careful calibration of the inversion parameters (Hojat et al., 2025) to reduce inversion artifacts in the resistivity images. This was necessary to correctly represent the real resistivity variations with time. Then we discuss how we modelled seasonal variations of the soil temperature with depth in order to correct resistivity changes due to temperature variations. The main objective is to correctly analyze the influence of rainfall events and piezometric level variations on resistivity changes, with the ultimate purpose to monitor the slope behavior during the seasonal cycle and under different hydrogeological conditions. This analysis will be illustrated in section 4.

3.1 Overall data quality

ERT data used in this paper were measured every 12 hours and the system started measurements at 1:00 am and at 1:00 pm every day. In case of extreme events, the system can be remotely programmed to make further measurements. All meteorological variables except rainfalls and piezometric levels are measured every 10 minutes and stored on the cloud platform with ERT data. Rainfall data are available as cumulative values over 15 minutes, 3 hours, 6 hours, 12 hours and 24 hours prior to the ERT acquisition time. Piezometric levels are the instant values measured when resistivity data are streamed to the cloud.

The external conditions such as air temperature, cumulative rainfalls, and the frequency of train passages are different for ERT data measured during the day compared to those acquired at night. Trains are considered as possible sources of electromagnetic noise that can interfere with the resistivity instrumentation. While no trains normally pass in the study site at night, they can influence the final quality of ERT data measured during the day. Therefore, a general assessment of data quality was performed in the first two months to compare the data measured during the day with those measured at night. The goal was to explore whether the differences in the measured resistivity values were significant or could be ignored.

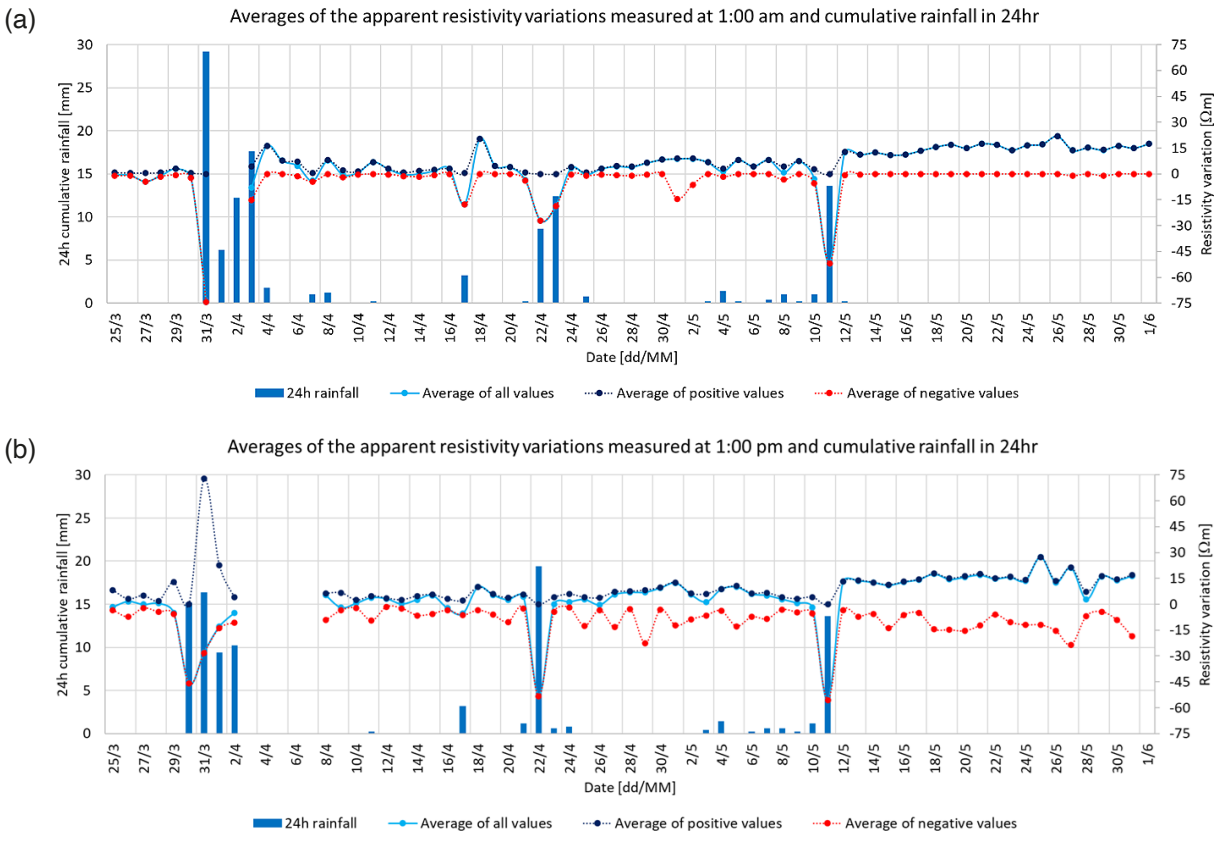

Figure 3. Trends of the average differences in apparent resistivity values measured in two successive days presenting the averages for all values, the positive values and the negative values. (a) nighttime data (measured at 1:00 am), (b) daytime data (measured at 1:00 pm). The vertical bars show the rainfall cumulated over 24 hr between each pair of resistivity measurements considered.

Figure 3 shows data trends for the nighttime and the daytime data along with rainfall events. Resistivity values are the average variations of the apparent resistivity values measured on two successive days at the same time, i.e., at 1:00 am for the nighttime data and at 1:00 pm for the daytime data, obtaining one value for each pair of days considered. Three graphs are illustrated on Fig. 3: average of positive variations, average of negative variations, and average of all variations. In order to distinguish the effects of rainfall events from the noise, the cumulated rainfalls over 24 hours between each pair of resistivity measurements were considered. Note that Fig. 3 presents two different datasets measured at two different times each day, i.e., data measured at 1:00 am versus data measured at 1:00 pm. Therefore, the reference time to calculate the cumulative rainfall is different for each graph and thus, rainfall values are not the same on both graphs. The missing data during 01-07 April is due to some instrumentation problems.

We can observe in Fig. 3 the general expectation that the resistivity is decreased after rainfalls and only positive resistivity variations are registered when the soil is being dried. However, some random positive oscillations after rainfalls and negative oscillations during the dry periods are also observed on the graph for the data measured during the day. These oscillations were noticed to be caused by a random and non-predictable distribution of values larger than the mean within the apparent resistivity pseudosections. These values, predominantly negative, do not align with the meteorological conditions, indicating that the nighttime data exhibit greater stability and appear to be more consistent with the dry periods' conditions. Therefore, although the overall trend observed on both datasets correctly reflects the rainfall events, we performed the long-term analysis using nighttime data which are basically free of noisy oscillations.

3.2 Inversion optimization

Having verified the better quality of nighttime data compared to daytime data, apparent resistivity data coming from 1:00 am surveys were inverted using the Res2DInvx64 software (Copyright © Seequent Systems, Incorporated). The raw data measured in an ERT survey are the apparent resistivity values that will be transformed to the real resistivity values through an inversion algorithm that searches for a subsurface resistivity model for which the calculated response matches the measured apparent resistivity data. As many other geophysical problems, ERT inverse problem is inherently nonlinear and ill-posed resulting in different model parameters that produce almost the same experimental observations (Loke et al., 2003, 2022a,b; Aleardi et al., 2022; Vinciguerra et al., 2022). Some studies are reported to observe minor differences between individual or time-lapse inversions of long-term ERT monitoring data, but there are several cases where a time-lapse inversion algorithm is necessary to avoid artifacts (Kim et al., 2009). This is due to the fact that no constraints are included on resistivity changes in the time direction when individual inversion is applied. When the subsurface is basically homogeneous or showing smooth variations of porosity and permeability, the difference between individually inverting the ERT monitoring data or using constrained time-lapse inversions might be negligible (Hojat et al., 2025), but the study site presented in this paper is a case where the complex subsurface geology resulted in the production of significant inversion artifacts when using individual or non-optimal time-lapse inversion algorithms. Preliminary inversion controls of the monitoring data measured before and after the first rainfall and drying periods in the study site showed that, due to the complex subsurface geology, strong artifacts appear on resistivity images when applying the individual or sub-optimal time-lapse inversions. Figure 4 illustrates an example section showing the percentage resistivity changes of the data measured on 04 and 05 November 2022 that were inverted separately. The rain gauge of the monitoring system registered 21.4 mm of rain in this timespan and thus, we would expect a completely negative section for resistivity

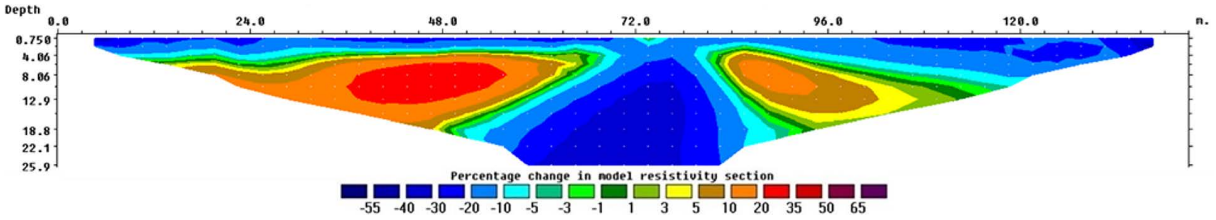

Figure 4. An example of percentage resistivity changes obtained from individual inversion of the data acquired on 04 and 05 November 2022, after 21.4 mm of rainfall.

changes, with higher variations in the shallowest layers and in the central higher-permeable-zone. Instead, on Fig. 4 we observe the expected behavior only in the central part of the profile while, contrary to real expectations, the lateral parts register significant positive resistivity changes approaching more than 20%. This kind of artifacts (with the opposite signs for resistivity variations) was also observed during the drying periods, again resulting in misleading reflection of the behavior of the side zones. The large resistivity contrasts between the higher permeable central zone and its lateral parts result in the production of artifacts in temporal images (Loke et al., 2022a).

Hojat et al. (2025) followed a forward modelling strategy to explore the nature of inversion artifacts and to compare individual versus time-lapse inversions for ERT monitoring data in the study site. Forward modeling tests confirmed the presence of significant inversion artifacts when individually inverting the data and the results showed the necessity of using a time-lapse inversion algorithm and correctly tuning the time-lapse damping factor with the spatial and temporal roughness constraints. Inversion artifacts were significantly reduced to less than 5% using a time-lapse damping factor of 5 and applying the smooth (L2 norm) and the robust/blocky (L1 norm) constraints for the spatial and temporal roughness, respectively. Figure 5 represents the same section shown in Fig. 4, but inverted using the time-lapse algorithm with optimized parameters. We can now observe on Fig. 5 that the entire section has negative or null resistivity variations with the major values concentrated down to 4 m in the higher-permeable soil and in the central part.

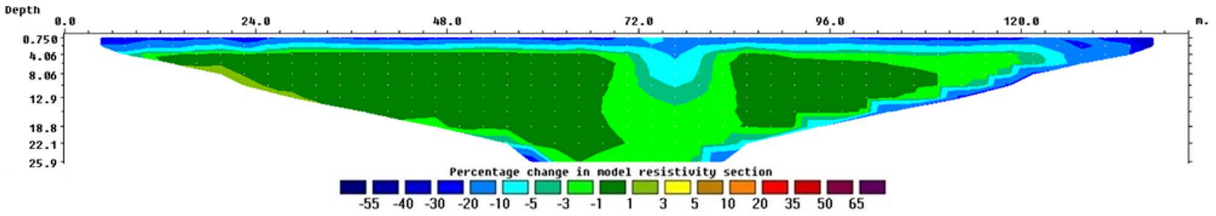

Figure 5. Percentage resistivity changes obtained from optimized time-lapse inversion of the data acquired on 04 and 05 November 2022, after 21.4 mm of rainfall (compare with Fig. 4).

3.3 Temperature correction

Since the electrical resistivity also depends on temperature, soil temperature is an important factor that influences seasonal analysis of ERT monitoring data. While temperature variations might affect the resistivity values only down to a couple of meters for short monitoring periods, resistivity changes due to soil temperature variations as deep as 5 m might become important when analyzing long-term ERT monitoring data (Hayley et al., 2007, 2010; Chambers et al., 2014). Therefore, a model for seasonal variations of the soil temperature at different depths should be developed (e.g., Brunet et al., 2010; Chambers et al., 2014; Bièvre et al., 2021). We used all the available data (March 2022-September 2023) of the air temperature sensor and the soil temperature sensor buried at 1.5 m depth to calibrate the site-specific relationship between the air temperature and the soil temperature at different depths. Eq. (1), used by many authors (e.g., Brunet et al., 2010; Chambers et al., 2014), could provide the modelled soil temperatures that fit well with our data:

$$T(z,t) = T_{mean}(air) + Ae^{-(z/d)} \sin(\omega t + \Phi - kz/d) \quad (1)$$

where T(z,t) is the modelled soil temperature at depth z and on day t of the year (t is in the range 1-365), Tmean(air) is the mean air temperature along the entire year, A is the maximum variation from the mean temperature, ω is the angular frequency (ω = 2π/(365)), Φ is the phase and k is a constant. The factor d is the characteristic penetration depth of temperature variations and is one of the unknowns to be calibrated along with A, Φ and k. A and Φ were calibrated at z = 0 m which corresponds to applying the model to air temperature data. d and k were then obtained from calibrating the model at z = 1.5 m where temperature measurements from the soil temperature sensor were available. The results of model calibration are shown in Fig. 6. We can observe a good fit between the modelled

soil temperature with the measured soil data, especially during the autumn and early spring and during the period July-September 2023. Modelled soil temperatures during winter tend to be slightly lower than the measured ones, given the mild climate registered in that season in 2022-2023, also shown by the higher air temperatures compared to the air simulated temperatures. Summer 2022 and late spring 2023 are the periods when the difference between the modelled and the measured temperatures is the highest. The model underestimates soil temperatures in summer 2022 while it overestimates soil temperatures in late spring 2023. However, the maximum difference between model and experimental data is less than 3.1°C, so that we decided to accept this model to calculate the temperature corrections at different depths.

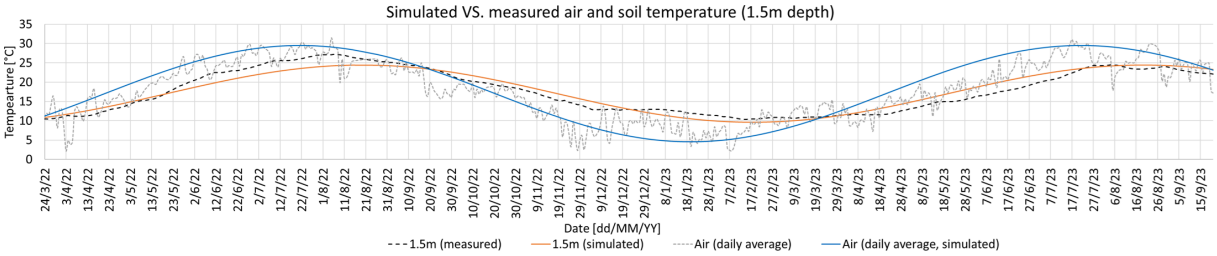

Figure 6. The measured (black dotted) and the modelled (orange) soil temperatures at 1.5 m depth along with the measured (grey dotted) and the modelled (blue) daily average air temperatures during March 2022-September 2023.

The soil temperature variations obtained from the calibrated model at different depths are shown in Fig. 7. We considered the depths compatible with the depth layers of the inverted resistivity models. We can realize on Fig. 7 that the soil temperature variations at about 4 m are already strongly damped and at 8 m are quite negligible. The overall response of the soil temperature to the air temperature in the study site seems limited to 6 m deep.

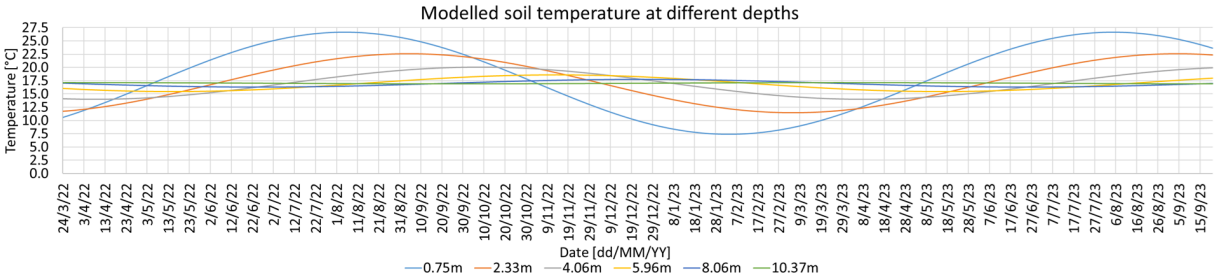

Figure 7. Modelled soil temperatures at different depths during March 2022-September 2023.

Having modelled the seasonal variations of the soil temperature, the inverted resistivity values were then corrected using Eq. (2) (Hayley et al., 2007):

$$\rho_{T_{mean}} = \rho_T\left(1 + \alpha(T - T_{mean})\right) \quad (2)$$

This equation allows to transform each resistivity value measured at any arbitrary temperature T (ρT) into the resistivity value for a reference temperature T_{mean} (ρT_{mean}). α is the coefficient of resistivity variations with temperature and is equal to 0.02°C-1. The reference T_{mean} temperature of 17°C was selected in our study, representing the mean air temperature during the calibration period. Table 1 reports the maximum corrections applied to different layers of the inverted resistivity model obtained from Eq. (2) and for the dates when temperature deviations from the mean value were maximum. Compatible with what we observed on Fig. 7, only the shallowest layers are

significantly affected by soil temperature variations and the resistivity corrections are lower than the background noise (about 2%) for the layers deeper than 5.96 m. Based on the results of this section, the target zones that will be discussed later were mostly not influenced by soil temperature variations; nonetheless, the corrections were still applied for completeness purposes.

Layer of the resistivity model	Depth of the midpoint of the layer	Maximum resistivity correction (from Eq. (2))
Layer 1	0.75 m	19.4%
Layer 2	2.32 m	11.2%
Layer 3	4.06 m	6.1%
Layer 4	5.96 m	3.2%
Layer 5	8.06 m	<2%

Table 1. The maximum resistivity corrections for the shallowest five layers of the inverted resistivity model.

4. Data analysis

4.1 Rainfalls and piezometric levels

Long-term analysis of the resistivity sections in response to rainfalls was carried out in comparison with the variations of the piezometric levels with the final goal to validate time-lapse ERT as a comprehensive tool for monitoring the slope behavior. As a typical example of rainfall effects, Fig. 8 illustrates the inverted resistivity sections for the data measured on 25 and 26 September 2022 before and after a rainfall event (63 mm cumulated rainfall). In order to make comparisons with the piezometric data, the positions of the five piezometers are also inserted on the ERT sections and the piezometric levels are shown by small black rectangles at the location of each piezometer. The third image on Fig. 8 shows the percentage changes in resistivity values and the immediate effect of rainfall in reducing the resistivity values is well observed down to 4 m. The subsurface material at this shallow part is composed of permeable topsoil. Below the top soil, we generally observe a different behavior of the site between the left side where S4 and S3 are positioned and the central and right regions where S5, S1 and S2 are located. On the left side of the profile and mainly due to the massive presence of clays and stone blocks, the resistivity values are high and we observe on the percentage change image that the resistivity response to rainfall is slow and approaches about −20%. In the central area between S5 and S1 and partially to the right of S1, the resistivity values are much lower and we observe remarkable resistivity variations in response to rainfall down to the level indicated by the S5-S1-S2 piezometers. Below these levels, resistivity variations are still visible but tend to reduce to less than 10%. These observations suggest that this central area is much more permeable than the left side region, which is consistent with the geological model, showing the presence of alternating layers of sand and gravel in this part. Therefore, these permeable layers can still receive new infiltrating water above the piezometric levels and this is reflected by the corresponding resistivity decrease, while the fully saturated material below the piezometric levels cannot host more water and resistivity variations become negligible. To the right of S2, the resistivity values are high but resistivity variations in response to rainfall are around −30% suggesting that the material is relatively permeable.

Variations of the water levels in the five piezometers are reported in Fig. 9 along with the 24-hour cumulative rainfalls. As mentioned above, the left and the right sides of the profile have different behaviors and thus, we present two graphs due to the large differences in the piezometric levels. We can observe in Fig. 9 that each piezometer

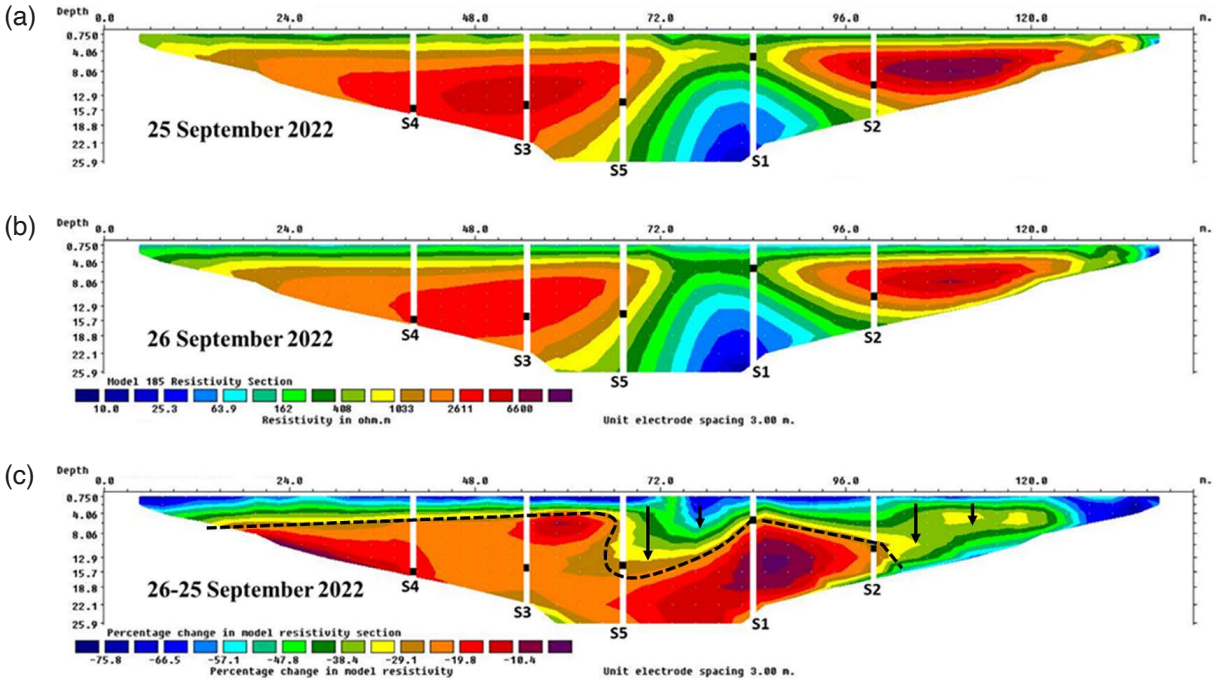

Figure 8. The inverted resistivity sections for the data measured before (25 September 2022) and after (26 September 2022) a rainfall event ((a) and (b), respectively) and their percentage difference (c). The black dashed line delimits the region that is registering a remarkable increase in water content while the black arrows mark the preferential infiltration paths through more permeable sediments.

responds differently to the meteorological events. S4 mainly reacts to intense rainfalls because it is surrounded by sandy-silt material. An abrupt decrease occurs in the water level measured in S4 on 21 November 2022, after which the water level tends to remain stable around 14.9 m even in the presence of heavy rainfalls. A possible explanation, that we cannot unfortunately confirm with other observations, is that one of the existing drainage wells installed in the past to reduce the hydrological pressure on the slope (the one closer to S4) was probably plugged, until the very intense rainfall on November 20 was finally able to reactivate it producing a sudden decrease in the piezometric level. The S3 piezometer is particularly stable and does not respond either to rainy events or to dry

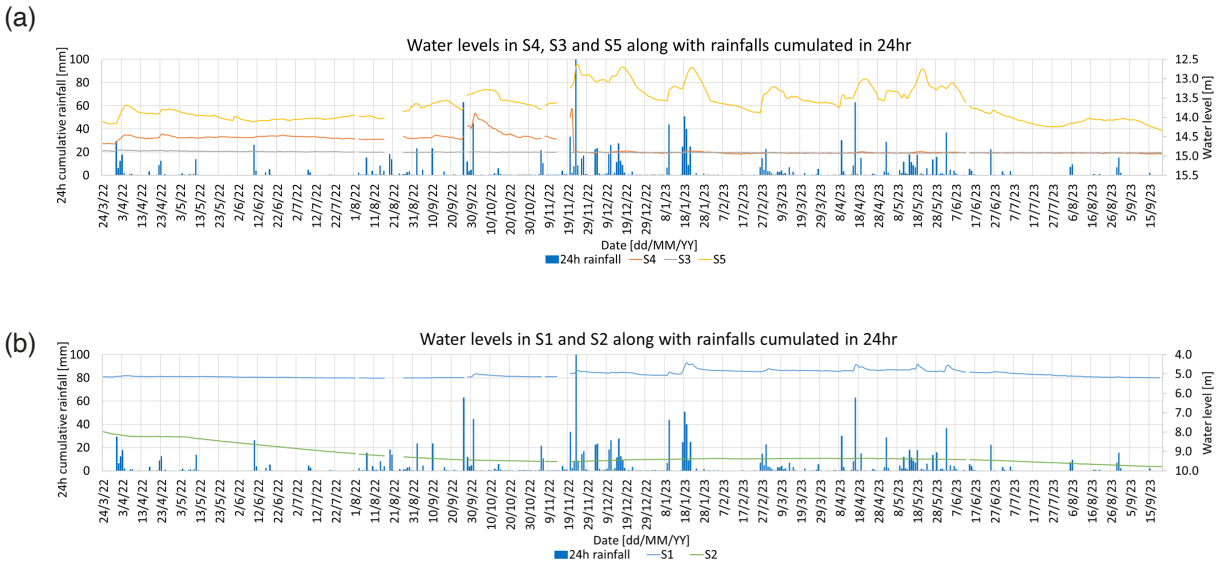

Figure 9. Water depth levels monitored by piezometers S4, S3, S5 (a) and S1, S2 (b) from 24 March 2022 until 21 September 2023, reported with the cumulated rainfall in 24 hr.

periods. This behavior is compatible with the low permeability of the clayey-loamy matrix around this piezometer. The central piezometer S5, on the other hand, is the one that responds most rapidly and significantly to rainfalls, with the water table that rises about 1 m in some periods. This is consistent with the presence of the higher permeable material in this central part of the section. Moving to the right side of the profile, S1 remained more or less stable until mid-September, after which it started to respond to rainfalls, still not that strongly. Similar to S4, the stratigraphy hosting S1 is composed of sandy-silt layers, but compared to S4 there is a thicker layer of alteration of chaotic clays that might justify a lower permeability around the piezometer. Finally, piezometer S2 showed an anomalous behavior, with a mainly decreasing trend until mid-November 2022, when extreme rainfalls temporarily interrupted the descent. After that, the water level in S2 was almost stable during the relatively rainy winter and spring seasons and returned to gently decreasing at the beginning of the summer. In conclusion, despite the fact that the distance between successive piezometers is only about 15 m, we have observed that they react very differently to rainfalls, and we can also note that they measure quite different water levels. General piezometric levels in S4, S3 and S5 are in the order of 13-15 m while piezometers S1 and S2 normally measure shallower levels between 5-9.5 m. All this confirms again the complexity of the site geology.

Considering the complex behavior of the site and the different trends observed in different piezometers, a unique correlation between the resistivity values and the piezometric levels cannot be analyzed on the entire ERT image. It is rather necessary to define small sub-zones surrounding each piezometer with a vertical extension that includes the water level oscillations measured by the piezometer. Figure 10 illustrates two regions named RS1 and RS5 that were respectively defined around piezometers S1 and S5 at depths compatible with the average water levels measured in the respective piezometer. RS1 is positioned at the horizontal distance 81 m-87 m along the profile and is extended at depth from 3.2 m to 5 m. RS5 has a similar lateral width and is horizontally positioned from 66 m to 72 m along the profile covering the depth range from 11.6 m to 14.2 m.

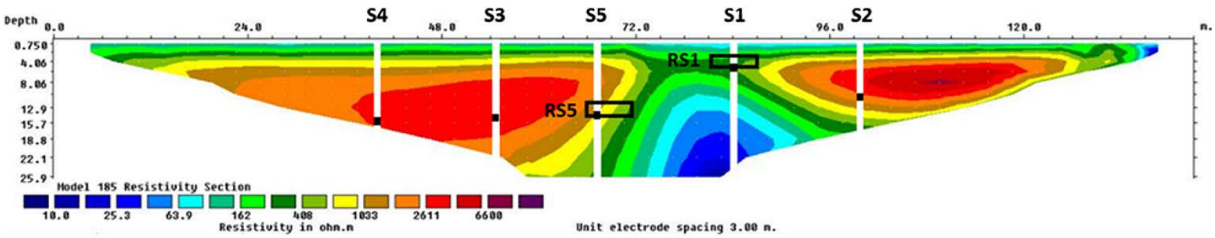

Figure 10. Subzones RS1 and RS5 defined along the ERT profile to study the correlations with the piezometers S1 and S5, respectively.

Figure 11 illustrates the average inverted resistivity values within the RS1 region in comparison with the cumulated rainfalls in 24 hr (Fig. 11a) and the water levels measured in S1 (Fig. 11b). The average resistivity is fairly constant in spring 2022 (March-May) and it increases in the summer due to the absence of rainfalls, showing that the effect of drought dominates the effect of temperature. In August 2022, when several rainfalls happen, the average resistivity begins to decrease and then it increases again until the last week of September 2022 after which, it decreases due to some significant rainfalls. The average resistivity remains more-or-less constant during autumn characterized by moderate rainfalls until the very intense events on 20 and 22 November. After that, the rainfall intensity remains high, but the resistivity curve looks quite insensitive, probably due to the difficulty of the soil to dry out between rainfall events (because of low winter temperatures), as well as the corresponding difficulty of the soil to receive more water during rainfalls. This approximately stable trend of poor reactions to rainfalls continues until the second half of June 2023 when resistivity value is notably increased, showing again a trend similar to what was observed during the summer period in 2022. Comparing the plot of the average resistivity in RS1 with the piezometric level in S1, we observe a generally consistent behaviour showing high resistivities during the summer when the water level is below the RS1 zone, and low resistivities during the other seasons when the water level partially saturates the RS1 zone.

Similar comparisons of the average resistivity value within RS5 area with the rainfalls and the water levels in S5 are presented in Fig. 12. According to S5 measurements, the RS5 zone remains partially saturated for almost the

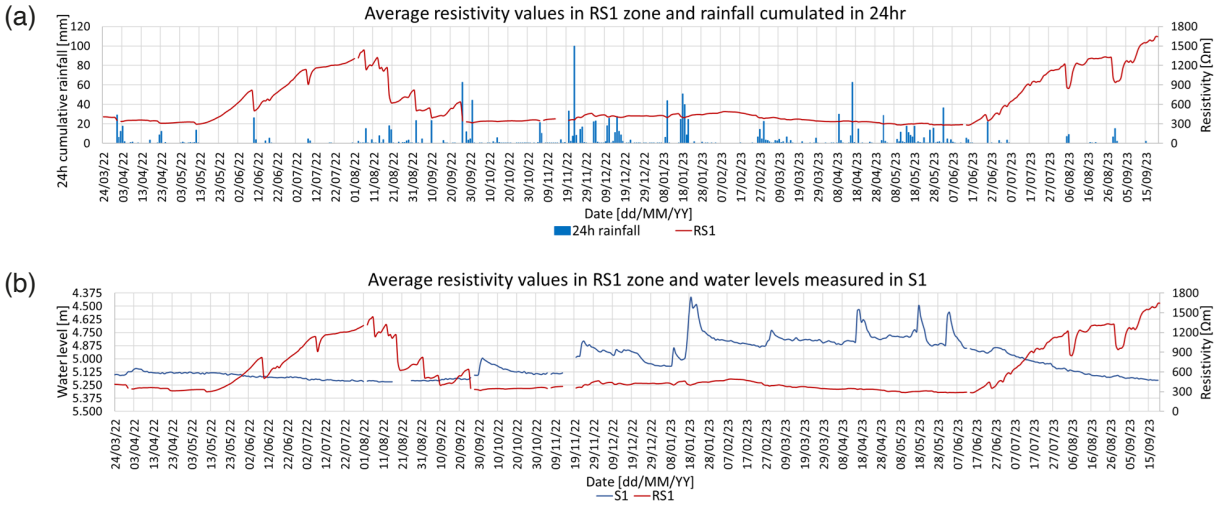

Figure 11. Average inverted resistivity values in the RS1 zone compared to cumulated rainfalls in 24 hr (a) and water depth levels recorded in S1 (b).

entire period, with the exception of the last 2 weeks in July 2023. The average resistivity value is increased during summer in 2022 and 2023 when RS5 becomes mainly dry. Similar to RS1, the resistivities in RS5 decrease after the rainfalls happening at the end of September 2022 and even more after the extreme rainfalls on 20 and 22 November. Then, the resistivity variations are correlated to rainfalls but poorly pronounced during the winter and spring seasons, probably due to a prolonged soil saturation caused by the difficulty of soil to dry at lower temperatures. The average resistivity is increased again after mid-June 2023, returning to high values as observed during the previous summer season. Overall, the general trends of the average resistivity values in RS5 and of the piezometric level in S5 show a clear relation, although the piezometer seems to be more sensitive to rainfalls during the winter and the spring.

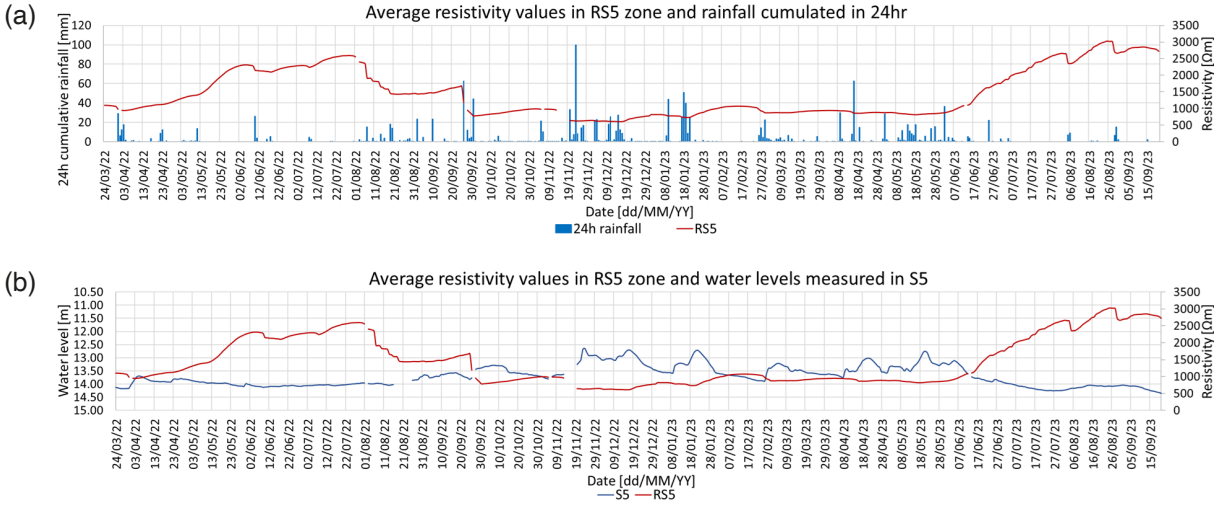

Figure 12. Average inverted resistivity values in the RS5 zone compared to cumulated rainfalls in 24 hr (a) and water depth levels recorded in S5 (b).

Both RS1 and RS5 have shown the rather poor reaction of the inverted resistivities to rainfalls during the winter, when temperatures are low and the soil maintains a high level of saturation because of frequent rainfalls as well as low temperatures. This is a general behavior that we can observe on all resistivity sections, as proved for example by comparing the inverted resistivity sections measured before and after the rainfalls on 22 November (Fig. 13).

Despite about 100 mm of rainfall registered, the entire section shows a limited resistivity decrease. The largest variations are still observed in the middle part where S5 is located, but they reach only the maximum 3% while the rest of the profile shows values smaller than 1.6%.

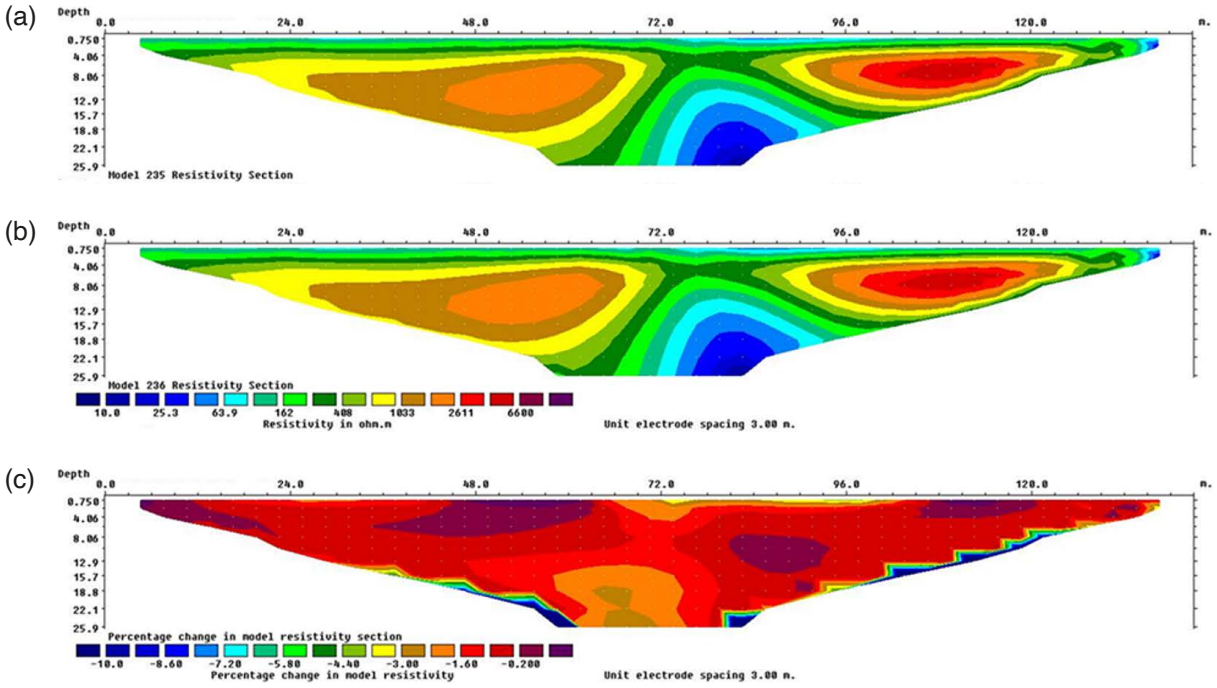

Figure 13. Inverted resistivity sections on 22 November 2022 (a) and 23 November 2022 (b) and section showing the percentage resistivity changes between the two days after 100 mm of rainfall (c).

4.2 Seasonal trends

By analyzing the entire monitoring period, it was possible to observe that the resistivity sections present a clear seasonal behavior, showing similar distributions over the sections according to the dominant meteorological condition and, accordingly, to the average piezometric levels of a certain period of the year. To illustrate the seasonal trend, we selected a few representative sections. Figure 14a is the typical section that can be observed during the summer season. Resistivity values are high due to the scarcity of rainfalls, which also caused the water levels to be decreased to their minimum. The area between S5 and S1 is the most conductive part in accordance with the geological model. During autumn, represented in Fig. 14b, rainfalls cause a visible decrease in resistivities compared to resistivity values measured in summer. This can be particularly observed in the first 4 m of soil, in the central area around S1 and also in the area to the right of S2, where values drop from over 6000 Ωm to less than 2600 Ωm. The winter season (Fig. 14c) was still characterized by rainfalls, but the decrease in resistivity values is less pronounced compared to the previous season, and is mainly registered in the left part of the section, confirming that this side of the section is characterized by low permeability material that needs a longer time to arrive at full saturation compared to other parts. Moreover, this period was characterized by a high stability in time, as could be seen from the graphs in Fig. 11 and Fig. 12. As discussed earlier, this was the effect of the prolonged saturation condition of the soil. Figure 14d shows the behavior of the site during spring. This section resembles the one observed in autumn due to a similar rainfall pattern. The last section (Fig. 14e), acquired in August 2023, replicates the typical summer behavior, showing a tomographic image extremely similar to the one observed in 2022. Again, the resistivities reach their peak values during this season.

On the whole, the seasonal trend of the tomographic images is consistent with the complex geological model and particularly with the different permeability properties already pointed out discussing the geological model and the response of resistivity to rainfall events.

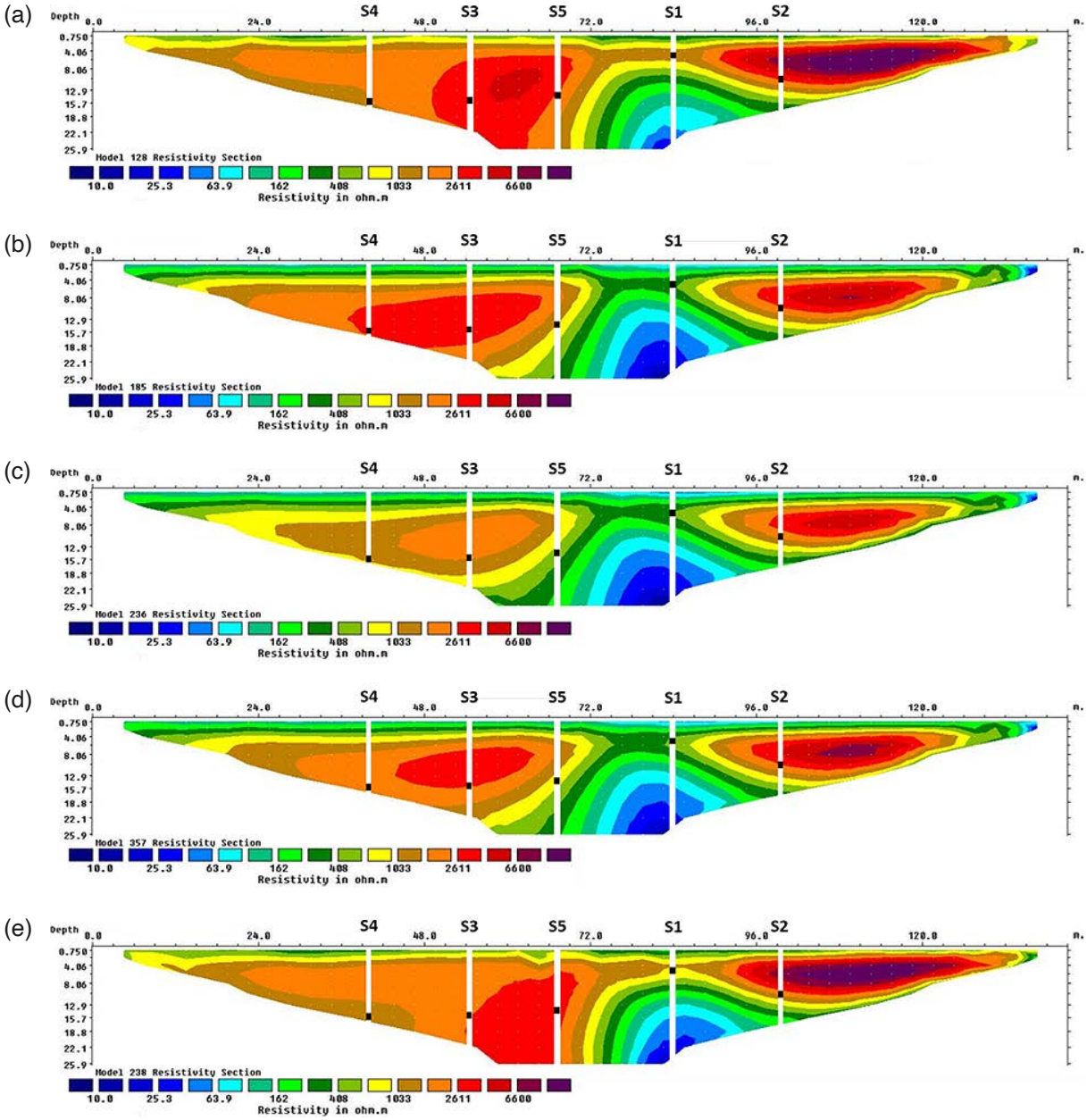

Figure 14. Inverted resistivity sections on: (a) 30 July 2022 (summer behavior), (b) 26 September 2022 (autumn behavior), (c) 23 November 2022 (winter behavior), (d) 24 March 2023 (spring behavior), (e) 27 August 2023 (summer behavior).

4.3 Preliminary definition of a warning threshold

Piezometric data measured along the ERT profile revealed a heterogeneous behavior of the site, especially in the area between S5 and S1. To analyze the correlation of these trends with the resistivity variations, we focused the attention on two small zones around these two piezometers: RS1 zone that surrounds the S1 piezometer, which shows the shallowest piezometric levels, and RS5 zone that surrounds the S5 piezometer, which seems to be the most sensitive to rainfalls. Our analysis, discussed in section 4.2, showed that the general trends of the average resistivity values in RS1 and RS5 agree with the general trends of the piezometric levels in S1 and S5, respectively. To further explore the trends, Fig. 15 shows the scatterplot of the daily pairs of the average resistivity values within RS5 and the water levels in S5. We use different colors to distinguish different time periods to help observing the different trends associated with the dominant meteorological and seasonal conditions. Two main trends can be distinguished on the scatter plot. One trend is observed in the lowest part of the plot that covers the summer and the spring data in 2022

plus the summer data in 2023. These data are characterized by low water levels due to the scarce rainfalls and high resistivity values ranging from 1000 Ωm to about 3000 Ωm. As expected, the correlation is negative (anticorrelation) if we refer to the water table elevation, and it is characterized by a gentle slope, which indicates a good sensitivity of the resistivity to water level variations. The only exception in this spring-summer period is observed for the data measured from 26 August until 25 September 2022, which follows its own trend. This exception is probably related to a malfunction of the system, which required a few maintenance interventions during that period. In fact, the box housing the system electronics had been tampered by unknown individuals and left open one week before the anomalous period. As a result, rain filtered inside the box, causing the need for subsequent interventions to replace some partially damaged components. The second trend that can be distinguished on the scatter plot is observed on the left part and covers the autumn, winter and spring periods from the end of September 2022 to mid-June 2023. This was a long period of moderate-to-high rainfalls, preceded and followed by drier periods. In this part we observe that the water table rises due to the abundant rainfalls and the resistivity values decrease accordingly. The anticorrelation slope is much more pronounced, indicating weaker sensitivity of the resistivity to water level variations. We observe that the transition between the two distinguishable regions of the scatter-plot is quite well defined by the intersection point of the two orthogonal red lines drawn on Fig. 15. This suggests defining a provisional pair of thresholds that might be used to activate an attention warning, e.g., 13.6 m for the water level in S5 and 960 Ωm for the average resistivity in RS5, meaning that we are entering the period of high saturation of the monitored slope. Further research is still needed to define the instability alarms in the study site. Aside from all monitoring data, all the information obtained from the preliminary geophysical and drilling exploration activities must be used along with the laboratory experiments on soil samples to define an accurate model for a geotechnical modelling software to evaluate what could be the physical conditions capable of producing the slope instability and what could be the resistivity and piezometric levels associated with the instability conditions. Therefore, the scatter plot shown in Fig. 15 only represents an intermediate result that encourages further research. In fact, the plot resembles the typical empirical behavior observed by other research groups when they plot the water content versus the inverted resistivity measured in similar geological environments (Doussan and Ruy, 2009; Tresoldi et al., 2019; Holmes et al., 2022). Based on this similarity, we tried to fit the scatter plot with a mathematical equation inspired by the relation proposed by Waxman and Smits (1968), also adopted by other researchers (e.g., Gunn et al., 2015; Onovughe and Sofolabo, 2016; Sam-Marcus et al., 2018), to extend the Archie's law (developed for granular materials like sands and gravel) to take into account the additional contribution to the conductivity produced by the clay matrix. In this exercise we use the water levels measured by the piezometer as a proxy of the water saturation that actually appears in the Waxman and Smits equation. Although this substitution is rather questionable, the resulting curve fits quite well the scatterplot and better results can be expected if real water saturation data could be used instead of the piezometric water levels. The curve has a less pronounced slope than actual data in the left part, while in the right part it has a better fitting due to the minor dispersion of the values. The pair of the thresholds previously individuated is also intersected by the curve, confirming it as a relevant point.

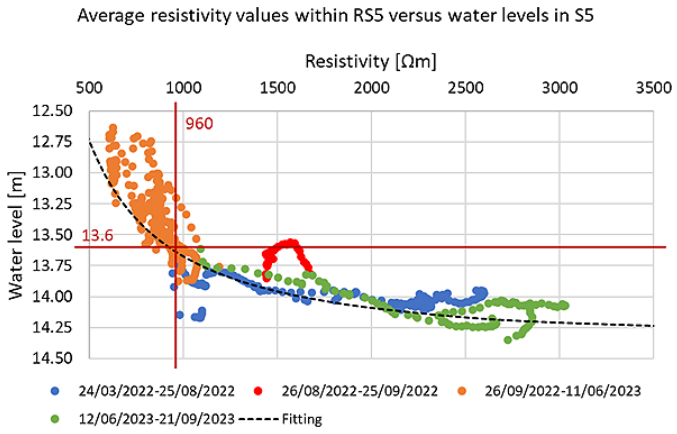

Figure 15. Scatterplot between the average resistivity values within the RS5 zone and the piezometric depth levels recorded in S5. Red lines roughly separate two distinguishable zones of the scatter plot. The dashed black curve is inspired by the Waxman and Smits relation (1968), although using the water level in substitution of the water saturation.

5. Conclusions

Long-term analysis of the ERT monitoring data on a critical slope above a high-speed railway tunnel has provided valuable insights into the hydrogeological dynamics of the site.

The complexity of the geological model and the variability of the site posed significant challenges in data processing and interpretation. The decision to move from individual inversion of the daily apparent resistivity pseudosections to a time-lapse inversion approach and the careful calibration of the inversion parameters were crucial steps in ensuring accurate representation of the resistivity variations with time.

A model of seasonal variations in soil temperature was calibrated to remove the temperature influence on resistivity measurements, ensuring a correct quantification of the resistivity values down to six meters of depth. According to the model, layers deeper than that do not require any temperature correction.

Integration of ERT monitoring with a meteorological station allowed comprehensive analysis of the site's response to environmental factors, particularly rainfall events. Comprehensive analysis of the resistivity maps in response to rainfalls integrated with the variations in piezometric levels exhibits a complex spatial distribution influenced by the heterogeneous geological composition of the site. The analysis of the entire monitoring period reveals clear seasonal trends in resistivity sections, reflecting the dominant meteorological conditions and the corresponding variations in piezometric levels. During summer, maximum values of the resistivity are recorded due to minimal rainfalls and the corresponding decrease in water levels, while autumn and spring exhibit decreased resistivity values attributed to distributed rainfalls. Winter, characterized by prolonged saturation, displays relatively stable resistivity patterns. These seasonal variations are consistent with the complex geological model and underscore the influence of permeability properties on resistivity responses to meteorological conditions.

The correlation between the resistivity values and the piezometric levels highlights the importance of localized analysis, necessitating the delineation of small sub-zones around piezometers for accurate interpretation. Focusing the analysis on specific target zones identified from ERT images proved more effective than analyzing the average resistivity behavior. This approach facilitated the establishment of preliminary thresholds for activating an early warning system addressing excessive water contents. However, further research is necessary to refine these thresholds and develop accurate geotechnical models for instability alarms.

In summary, the long-term analysis of ERT monitoring data has demonstrated its effectiveness in understanding the complex hydrogeological dynamics of the critical slope. By overcoming the technical challenges and integrating the ERT data with meteorological data, ERT monitoring offers valuable support for informed decision-making and risk management in infrastructure projects such as high-speed railways.

Data availability statement. Data sets used in this paper belong to a private entity and are not permitted to be shared.

Acknowledgements. The ERT monitoring system is developed by LSI LASTEM s.r.l. with scientific support of Politecnico di Milano. Inversion of ERT data was generated using Seequent Res2dinvx64 Software (Copyright © Seequent Systems, Incorporated).

References

Aleardi, M., A. Vinciguerra, E. Stucchi and A. Hojat (2022). Probabilistic inversions of electrical resistivity tomography data with a machine learning-based forward operator, Geophys. Prospect., 70, 5, 938-957, doi:10.1111/1365-2478.13189.

Amitrano, D., M. Arattano, M. Chiarle, G. Mortara et al. (2010). Microseismic activity analysis for the study of the rupture mechanisms in unstable rock masses, Nat. Hazards Earth Syst. Sci., 10, 4, 831-841, doi:10.5194/nhess-10-831-2010.

Bièvre, G., D. Jongmans, T. Lebourg and S. Carrière (2021). Electrical resistivity monitoring of an earthslide with electrodes located outside the unstable zone (Pont-Bourquin landslide, Swiss Alps), Near Surf. Geophys., 19, 2, 225-239, doi:10.1002/nsg.12145.

Brunet, P., R. Clément and C. Bouvier (2010). Monitoring soil water content and deficit using Electrical Resistivity Tomography (ERT) – A case study in the Cevennes area, France, J. Hydrol., 380, 1-2, 146-153, doi:10.1016/j.jhydrol.2009.10.032.

Chambers, J. E., P. I. Meldrum, D. A. Gunn, P. B. Wilkinson et al. (2009). Hydrogeophysical monitoring of landslide processes using automated time-lapse electrical resistivity tomography (ALERT), 15th EAGE European Meeting of Environmental and Engineering Geophysics, Dublin, Ireland, doi:10.3997/2214-4609.20147066.

Chambers, J. E., D. A. Gunn, P. B. Wilkinson, P. I. Meldrum, E. Haslam et al. (2014). 4D electrical resistivity tomography monitoring of soil moisture dynamics in an operational railway embankment, Near Surf. Geophys., 12, 1, 61-72, doi:10.3997/1873-0604.2013002.

Chambers, J., J. Holmes, J. Whiteley, J. Boyd et al. (2022). Long-term geoelectrical monitoring of landslides in natural and engineered slopes, The Leading Edge, 41, 11, 742-804, doi:10.1190/tle41110768.1.

Dahlin, T., V. Leroux, R. Larsson and K. Rankka (2005). Resistivity imaging for mapping of quick clays for landslide risk assessment, 11th European Meeting of Environmental and Engineering Geophysics, Palermo, Italy, doi:10.3997/2214-4609-pdb.13.A046.

Doussan, C. and S. Ruy (2009). Prediction of unsaturated soil hydraulic conductivity with electrical conductivity, Water Resour. Res., 45, 10, W10408, doi:10.1029/2008WR007309.

Geotomosoft web portal (http://geotomosoft.com; www.aarhusgeosoftware.dk).

Gunn, D. A., J. E. Chambers., S. Uhlemann, P. B. Wilkinson et al. (2015). Moisture monitoring in clay embankments using electrical resistivity tomography, Constr. Build. Mater., 92, 82-94, doi:10.1016/j.conbuildmat.2014.06.007.

Hayley, K., L. R. Bentley, M. Gharibi and M. Nightingale (2007). Low temperature dependence of electrical resistivity: Implications for near surface geophysical monitoring, Geophys. Res. Letters, 34, 18, L18402, doi:10.1029/2007GL031124.

Hayley, K., L. R. Bentley and A. Pidlisecky (2010). Compensating for temperature variations in time-lapse electrical resistivity difference imaging, Geophys., 75, 4, WA51-WA59, doi:10.1190/1.3478208.

Hojat, A. (2024). An iterative 3D correction plus 2D inversion procedure to remove 3D effects from 2D ERT data along embankments, Sensors, 24, 12, 3759, doi:10.3390/s24123759.

Hojat, A., G. Tresoldi and L. Zanzi (2021). Correcting the effect of the soil covering buried electrodes for permanent electrical resistivity tomography monitoring systems, 4th Asia Pacific Meeting on Near Surface Geoscience & Engineering, Online, doi:10.3997/2214-4609.202177070.

Hojat, A., L. Zanzi, G. Tresoldi and M. H. Loke (2025). Forward modelling simulations to validate changes in electrical resistivity tomography monitoring data for a slope with complex geology, Geosciences, 15, 1, 33, doi:10.3390/geosciences15010033.

Holmes, J., J. Chambers, P. Wilkinson, B. Dashwood et al. (2022). 4D electrical resistivity tomography for assessing the influence of vegetation and subsurface moisture on railway cutting condition, Eng. Geol., 307, 106790, doi:10.1016/j.enggeo.2022.106790.

Kim, J. H., M. J. Yi, S. G. Park and J. G. Kim (2009) 4-D inversion of DC resistivity monitoring data acquired over a dynamically changing earth model, J. Appl. Geophys., 68, 522-532, doi:10.1016/j.jappgeo.2009.03.002.

Kuras, O., P. B. Wilkinson, P. I. Meldrum, R. T. Swift et al. (2015). Performance assessment of novel electrode materials for long-term ERT monitoring. Proceedings of the 21st European Meeting of Environmental and Engineering Geophysics, Turin, Italy, doi:10.3997/2214-4609.201413777.

Loke, M. H., I. Acworth and T. Dahlin (2003). A comparison of smooth and blocky inversion methods in 2D electrical imaging surveys, Explor. Geophys., 34, 3, 182-187, doi:10.1071/EG03182.

Loke, M. H., J. E. Chambers, D. F. Rucker, O. Kuras and P. B. Wilkinson (2013). Recent developments in the direct-current geoelectrical imaging method, J. Appl. Geophys., 95, 135-156, doi:10.1016/j.jappgeo.2013.02.017.

Loke, M. H., P. B. Wilkinson, J. E. Chambers, S. Uhlemann et al. (2022a). The use of asymmetric time constraints in 4-D ERT inversion, J. Appl. Geophys., 197, 104563, doi:10.1016/j.jappgeo.2022.104536.

Loke, M. H., P. B. Wilkinson, O. Kuras, P. I. Meldrum et al. (2022b). The use of a semi-structured finite-element mesh in 3-D resistivity inversion, Geophys. Prospect., 70, 9, 1580-1601, doi:10.1111/1365-2478.13260.

Moradipour, M., H. Ranjbar, A. Hojat, S. Karimi Nasab and S. Daneshpajouh (2016). Laboratory and field measurements of electrical resistivity to study heap leaching pad no. 3 at Sarcheshmeh copper mine, 22nd European Meeting of Environmental and Engineering Geophysics, Barcelona, Spain, doi:10.3997/2214-4609.201602140.

Onovughe, E. and A. Sofolabo (2016). Saturation modelling: using the Waxman-Smits model/equation in saturation determination in dispersed shaly sands, Journal of Multidisciplinary Engineering Science and Technology (JMEST), 3, 6, 4985-4992, ISSN:2458-9403.

Piegari, E., V. Cataudella, R. Di Maio, L. Milano et al. (2009). Electrical resistivity tomography and statistical analysis in landslide modelling: A conceptual approach, J. Appl. Geophys., 68, 2, 151-158, doi:10.1016/j.jappgeo.2008.10.014.

Sam-Marcus, J., E. Enaworu, O. J. Rotimi and I. Seteyeobot (2018). A proposed solution to the determination of water saturation: using a modelled equation, J. Petrol. Explor. Prod. Technol., 8, 1009-1015, doi:10.1007/s13202-018-0453-4.

Supper, R., D. Ottowitz, B. Jochum, J. H. Kim et al. (2013). Geoelectrical monitoring: an innovative method to supplement landslide surveillance and early warning, Near Surf. Geophys., 12, 1, 133-150, doi:10.3997/1873-0604.2013060.

Tresoldi, G., D. Arosio, A. Hojat, L. Longoni et al. (2018). Tech-Levee-Watch: experimenting an integrated geophysical system for stability assessment of levees, Rendiconti Online della Società Geologica Italiana, 46, 38-43, doi:10.3301/ROL.2018.49.

Tresoldi, G., D. Arosio, A. Hojat, L. Longoni, M. Papini and L. Zanzi (2019). Long-term hydrogeophysical monitoring of the internal conditions of river levees, Eng. Geol., 259, 105139, doi:10.1016/j.enggeo.2019.05.016.

Tresoldi, G., A. Hojat and L. Zanzi (2020). G.RE.T.A. installations for real-time monitoring of irrigation dams and canals, Procedia Environmental Science, Engineering and Management, 7, 2, 272-276.

Vinciguerra, A., M. Aleardi, A. Hojat, M. H. Loke and E. Stucchi (2022). Discrete cosine transform for parameter space reduction in Bayesian electrical resistivity tomography. Geophys. Prospect., 70, 1, 193-209, doi:10.1111/1365-2478.13148.

Watlet, A., H. Thirugnanam, B. Singh, N. M. Kumar et al. (2023). 4D electrical resistivity to monitor unstable slopes in mountainous tropical regions: an example from Munnar, India, Landslides, 20, 1031-1044, doi:10.1007/s10346-023-02029-3.

Waxman, M. H. and L. J. M. Smits (1968). Electrical conductivities in oil-bearing shaly sands, Soc. Petrol. Eng. J., 8, 2, 107-122, doi:10.2118/1863-A.

Whiteley, J. S., A. Watlet, J. M. Kendall and J. E. Chambers (2021). Brief communication: the role of geophysical imaging in local landslide early warning systems, Nat. Hazards Earth Syst. Sci., 21, 12, 3863-3871, doi:10.5194/nhess-21-3863-2021.

Wilkinson, P. B., J. E. Chambers, P. I. Meldrum, O. Kuras et al. (2022). Windowed 4D inversion for near real-time geoelectrical monitoring applications, Front. Earth Sci., 10, 983603, doi:10.3389/feart.2022.983603.

Wilkinson, P., J. Chambers, P. Meldrum, R. Swift et al. (2023). Trial of the PRIME system for geoelectrical condition monitoring on critical railway earthwork infrastructure, 29th European Meeting of Environmental and Engineering Geophysics, Edinburgh, United Kingdom, doi:10.3997/2214-4609.202320155.

Zhang, Z., D. Arosio, A. Hojat and I. Zanzi (2020). Tomographic experiments for defining the 3D velocity model of an unstable rock slope to support microseismic event interpretation, Geosciences, 10, 9, 327, doi:10.3390/geosciences10090327.

Zhang, Z., D. Arosio, A. Hojat and I. Zanzi (2021). Reclassification of microseismic events through hypocenter location: case study of an unstable rock face in Northern Italy, Geosciences, 11, 1, 37, doi:10.3390/geosciences11010037.

***CORRESPONDING AUTHOR: Azadeh HOJAT**,
Politecnico di Milano, Dipartimento di Ingegneria Civile e Ambientale, Piazza Leonardo da Vinci 32, 20133 Milano, Italy
e-mail: azadeh.hojat@polimi.it